Letters

Wide-Load Range Multiobjective Efficiency Optimization Produces Closed-Form Control Solutions for Dual Active Bridge Converter

Lu Zhou, *Student Member, IEEE*, Yihan Gao, Hao Ma, *Senior Member, IEEE*, and Philip T. Krein, *Fellow, IEEE*

***Abstract*—This letter proposes a multiobjective efficiency optimization method for triple-phase-shift (TPS) control of isolated dual active bridge converters (DABs). A comprehensive optimization of inductor current stress, inductor rms current, and zero-voltage switching (ZVS) is presented to reduce conduction losses, magnetic losses, and switching losses. A genetic algorithm is used to search for optimal solutions of the DAB nonconvex optimization problem. Analysis of these solutions gives rise to closed-form expressions for optimum TPS control angles, valid over various power and voltage levels. These can be realized for real-time operation. A 3.3-kW experimental prototype is used to verify the proposed optimized modulation control.**

***Index Terms*—Current minimization, dual active bridge converters (DABs), nondominated sorting genetic algorithm, rms current, triple-phase-shift (TPS) control, zero-voltage switching (ZVS).**

I. Introduction

THE vehicle-to-grid [1] concept implies bidirectional energy flow, so topologies such as dual active bridge converters (DABs) are of interest for electric charger interfaces. They provide galvanic isolation, high power density, the potential for zero-voltage switching (ZVS), wide output voltage range, and the potential for modularity.

Phase-shift control is a mainstream DAB method at present. Currents increase rapidly as the voltage conversion ratio moves away from unity in single-phase-shift control. Extended-phase-shift control, dual-phase-shift control, and triple-phase-shift (TPS) control [2]–[5] have been proposed to add degrees of freedom and overcome drawbacks of single-phase-shift control. In principle, a DAB offers up to four degrees of freedom: external phase-shift, internal phase-shift in the primary bridge, internal phase-shift in the secondary bridge, and frequency. Given the addition of frequency as a free parameter, TPS control covers all these possibilities, and is applied here.

Certain combinations of phase shifts in TPS control will have substantial impact on efficiency [6]–[8]. In previous works on DAB efficiency optimization, typically only one optimization goal was considered in addition to ZVS [2]–[4], [9]–[14], leading to reduction of only conduction loss or of magnetic loss. Consideration of conduction losses, magnetic losses, and switching losses together in a multiobjective model can serve as a basis for further efficiency improvement.

For optimization, Newton's method can be used when convex optimization problems satisfy Karush–Kuhn–Tucker (KKT) conditions [9]–[11]. Nonconvex optimization problems are difficult to solve. Particle swarm optimization (PSO) was used in [3] to achieve minimum current and to determine relationships between phase shifts and power delivery. Soft switching and minimum reactive power were not considered. PSO for minimum reactive power based on phasor analysis was presented in [4]. In nonconvex problems, iterative numerical calculation methods and PSO tend to get trapped near local solutions rather than locating the global optimum. In [14], a detailed loss model was presented, with efficiency and power density as the optimization goals. The use of GaN devices further improves the circuit performance. Solutions for DABs that use TPS control were presented in [5] and [12]. The phase-shift trajectory was stored in a multidimensional look-up table.

To optimize wide-load range efficiency, this letter seeks a multiobjective constraint model that can function in real time for TPS control. Optimization considers minimum inductor current, minimum inductor rms current, and a broadened ZVS region. Each of these is considered, in turn, to reduce conduction losses, magnetic losses, and switching losses. With these objectives and constraints, the NSGA-II method [15] is employed for nonconvex optimization and to explore Pareto fronts. The results lead to closed-form phase-shift formulas. These can be implemented in real time. The results are validated in an experimental DAB.

Manuscript received December 4, 2020; revised January 6, 2021; accepted January 21, 2021. Date of publication January 27, 2021; date of current version May 5, 2021. This work was supported in part by the Zhejiang University/University of Illinois at Urbana-Champaign Institute. *(Corresponding author: Hao Ma.)*

Lu Zhou and Hao Ma are with the College of Electrical Engineering, Zhejiang University, Hangzhou 310027, China, and also with the Zhejiang University/University of Illinois at Urbana–Champaign Institute, Haining 314400, China (e-mail: 11810047@zju.edu.cn; mahao@zju.edu.cn).

Yihan Gao is with the College of Electrical Engineering, Zhejiang University, Hangzhou 310027, China (e-mail: 21760557@zju.edu.cn).

Philip T. Krein is with the College of Electrical Engineering, Zhejiang University, Hangzhou 310027, China, with the Zhejiang University/University of Illinois at Urbana–Champaign Institute, Haining 314400, China, and also with the University of Illinois at Urbana–Champaign, Urbana, IL 61801 USA (e-mail: krein@illinois.edu).

Color versions of one or more figures in this article are available at https://doi.org/10.1109/TPEL.2021.3054970.

Digital Object Identifier 10.1109/TPEL.2021.3054970

TABLE I
WAVEFORMS AND PHASE-SHIFTS OF EIGHT FORWARD MODES IN TPS CONTROL

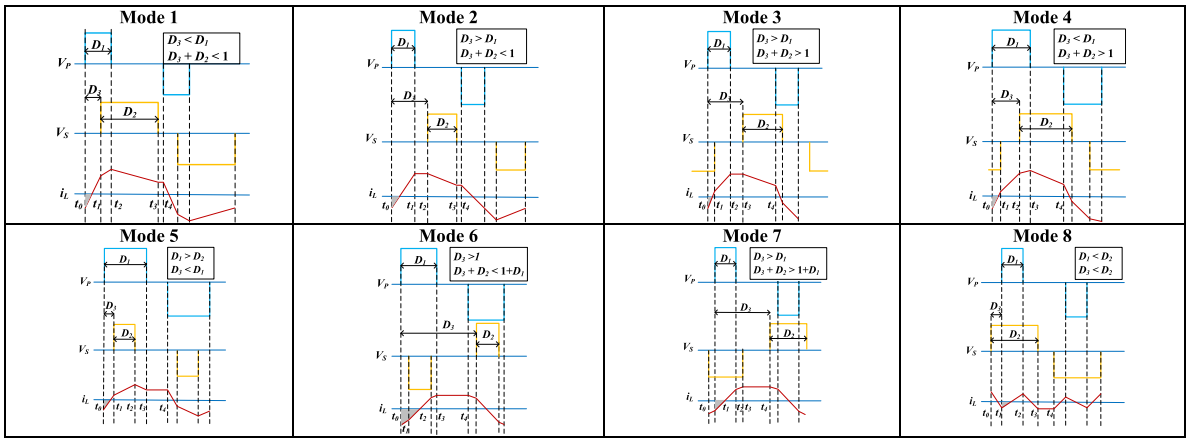

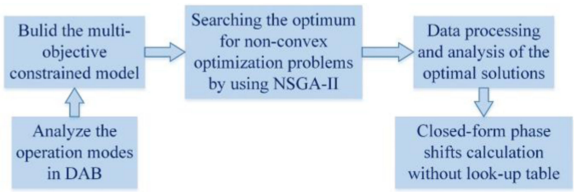

Fig. 1. Process of the proposed method.

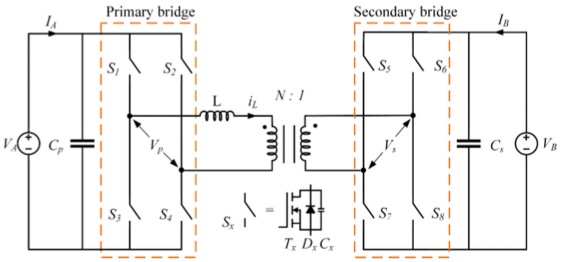

Fig. 2. DAB topology for this study.

II. DAB: OBJECTIVES AND CONSTRAINTS

A. Multiobjective Constraint Modeling of DAB

A block diagram of the method proposed here is shown in Fig. 1. The DAB topology employed here is shown in Fig. 2. S_X denotes the switches, each including active switch T_X, antiparallel diode D_X, and junction capacitance C_X. V_A and I_A represent the primary-side voltage and current, respectively. V_B and I_B represent the secondary-side voltage and current, respectively.

Consider TPS as a generalization of phase-control methods. Up to 12 operating modes can be addressed. The eight modes for forward transmission are depicted in Table I. D_1 and $D_2 \in [0,1]$ denote duty ratios on the primary and secondary sides, also referred to as internal phase shifts. D_3 denotes external phase shift. The voltage gain is $m = NV_B/V_A$. The case $m > 1$ ($m < 1$) represents boost (buck) mode. The analysis is similar, so only buck mode with $m < 1$ is discussed here.

To maximize overall conversion efficiency, conduction losses, magnetic losses, and switching losses are all considered. This letter uses rms current and peak current to represent conduction loss and magnetic loss. ZVS is considered to reduce switching loss. It is inaccurate to use reactive power as a surrogate for conduction losses, since reactive power and rms current are not strictly proportional. The multiobjective constraint model is

$$\begin{cases} Obj.1 = i_{stress}(V_A, V_B, D_1, D_2, D_3) \\ Obj.2 = I_{rms}(V_A, V_B, D_1, D_2, D_3) \\ Econst.1 = P_{trans}(V_A, V_B, D_1, D_2, D_3) \\ inEconst.1 = f_{limit}(D_1, D_2, D_3) \\ inEconst.2 = i_{min}(V_A, V_B). \end{cases} \tag{1}$$

Here, *Obj.1* is the inductor peak current, derived in the buck/boost mode. *Obj.2* is the primary-side inductor rms current. The average power delivered to the load is used as Econst.1 to ensure correct output. They are related to the input and output voltage and the phase-shift angles as follows:

$$\begin{cases} P_{\text{trans}} = 2f_S \int_{t0}^{t4} i_L(t) v_P(t)\, dt \\ I_{\text{rms}} = \\ \sqrt{2f_S\left[\int_{t0}^{t1} i_L(t)^2 dt + \int_{t1}^{t2} i_L(t)^2 dt + \int_{t2}^{t3} i_L(t)^2 dt + \int_{t3}^{t4} i_L(t)^2 dt\right]} \end{cases} \tag{2}$$

where f_s is the switching frequency, $v_P(t)$ is the time-varying primary midpoint voltage, and time interval t_0–t_4 captures a half cycle of the symmetrical waveforms.

Since different phase-shift angle relations form eight operating modes, the phase-shift angle is restricted in *inEconst.1* to divide the modes, as shown in Table I. The current boundary for soft switching is used as *inEconst.2*

$$I_{\min} = \sqrt{\left[2C_{\text{eq}}(V_{\text{DS}}) + C_{\text{par}}\right] {V_{\text{DS}}}^2 / L} \tag{3}$$

where C_{par} combines the parasitic capacitances of the PCB and inductor and C_{eq} is a nonlinear function of device voltage.

ZVS constraints are imposed on both the primary and secondary bridges. A charge-equivalent capacitance C_{eq} is used to model the process:

$$C_{\text{eq}} = \frac{Q_{\text{oss}}(V_{\text{DS}})}{V_{\text{DS}}} = \frac{\int_0^{V_{\text{DS}}} C_{\text{oss}}(v)\, dv}{V_{\text{DS}}} \tag{4}$$

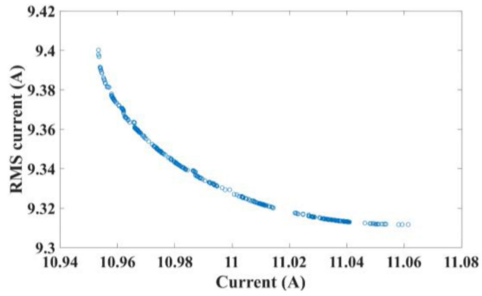

Fig. 3. Example of results from NSGA-II with $V_A = 400$ V, $V_B = 157$ V, and $P_{\rm trans} = 800$ W.

where $Q_{\rm oss}$ is the stored charge, $C_{\rm oss}$ is the nonlinear parasitic output capacitance, and $V_{\rm DS}$ is the switch drain–source voltage.

The required inductor energy can be determined from energy conservation. The minimum current for ZVS can be deduced as in (3). With nonlinear capacitances, the soft switching current boundaries on the primary side $I_{\rm sp}$ and secondary side $I_{\rm ss}$ are

$$\begin{cases} I_{\rm sp} = V_A\sqrt{\left[2C_{\rm eq}(V_A) + C_{\rm par}\right]/L} \\ I_{\rm ss} = V_B\sqrt{\left[2C_{\rm eq}(V_B) + C_{\rm par}\right]/L}. \end{cases} \tag{5}$$

B. Solve Multiobjective Nonconvex Optimization With NSGA

The model in (1) is nonconvex. Genetic algorithms can solve nonconvex optimization problems. The NSGA-II algorithm [15] has been relatively successful because of its low computational complexity, rapid convergence, ease of implementation, and broad applicability. NSGA-II uses crossovers, mutations, and nondominated sorting to generate new populations of solutions at each step. Simulated binary crossovers and polynomial mutations [16] are implied here.

In the case of low voltage and high current, conduction loss and magnetic loss account for a relatively large proportion of the total loss. In the case of high switching frequency, switching loss is proportionally higher. The rms current, peak current, and ZVS current are used to represent losses in this letter. Multiobjective optimization attempts to obtain a set of optimal tradeoff solutions, such as between peak current and rms current. The results can be displayed as Pareto frontiers, with an example shown in Fig. 3. This plot shows results for 453 solutions. Conduction losses account for more than 50% of total losses when ZVS is enforced [17]. The solution with minimum rms current is preferred to reduce conduction and magnetic losses. The TPS strategy supports eight modes for forward power delivery, as listed in Table I. Each one needs to be checked to find the optimum.

III. Optimized Closed-Form Calculation

The NSGA-II algorithm can be applied to explore (1). This can be carried out offline in MATLAB software. For control, the phase shifts can be solved at various voltage gains m associated with various power levels. The smaller the value of m, the lighter the load.

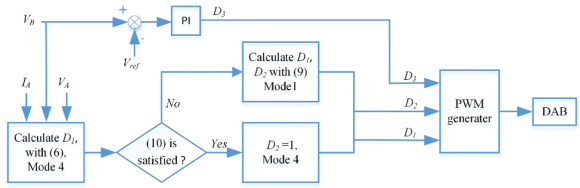

Fig. 4. Closed-form control block diagram.

Offline phase-shift solutions produce some interesting relationships, which are as follows.

1) Almost all optimal solutions are located in Mode 1, 4, and 8.
2) For Mode 1, almost all optimal solutions fall on the soft switching boundary.
3) For Mode 4, the secondary-side duty ratios are close to $D_2 = 1$.
4) Mode 8 is suitable for lower power due to its limits on maximum transferred power and soft switching.
5) Starting from high power, under a given voltage gain m, optimal solutions are usually located in Mode 4. Mode 1 becomes optimal as power decreases. Mode switching will occur when Mode 4 cannot enforce the secondary-side soft switching constraint with relatively low current and rms current.

Useful mathematical relationships among phase shifts can be obtained by fitting data from offline results. The variables are D_1, D_2, D_3, voltage gain m, and transferred power $P_{\rm trans\_x}$ (x denotes the operating mode).

For Mode 4, by using multiple linear regression, D_1 fits to

$$D_1 = 0.601 + 0.574m - 4096L - 4.996\times10^{-5}P_{\rm trans\_4} \tag{6}$$

with L in henries and P in watts. The correlation residuals $r = 0.9670$, $F = 234.3$, and $p = 0$ indicate that D_1 is linearly related to the independent variables.

In Mode 4, the best results have $D_2 \approx 1$. This result with that in (6) are new and nonobvious optimum results for TPS control. These linear expressions are obtained through data analysis of offline NSGA-II optima. This method implies rules among the values. The results can be exploited to yield closed-form relationships and to support real-time control.

An expression for D_3 in Mode 4 can be derived from the transfer power equation, since $D_2 = 1$, and

$$D_3 = D_1 - \sqrt{D_1 - P_{\rm trans\_4}/P_{\rm base}}. \tag{7}$$

In Mode 1, the duty ratios can be obtained by solving soft-switching boundary current and transfer power equations as follows:

$$I_0 = I_{\rm sp}, I_1 = I_{\rm ss}/N, P_{\rm trans} = P_{\rm trans\_1}. \tag{8}$$

The results are

$$\begin{cases} D_1 = \dfrac{\sqrt{2f_SL[P_{\rm trans\_1}m' + I_{\rm sp}^2(m' + \frac{m^3}{N^4})]} + 2f_SLI_{\rm sp}(m' - \frac{m^2}{N^2})}{m'V_A} \\ D_2 = \dfrac{D_1}{m} - \dfrac{4f_SLI_{\rm sp}}{mV_A}, D_3 = \dfrac{2f_SL(I_{\rm sp}+I_{\rm ss})}{V_A} \end{cases} \tag{9}$$

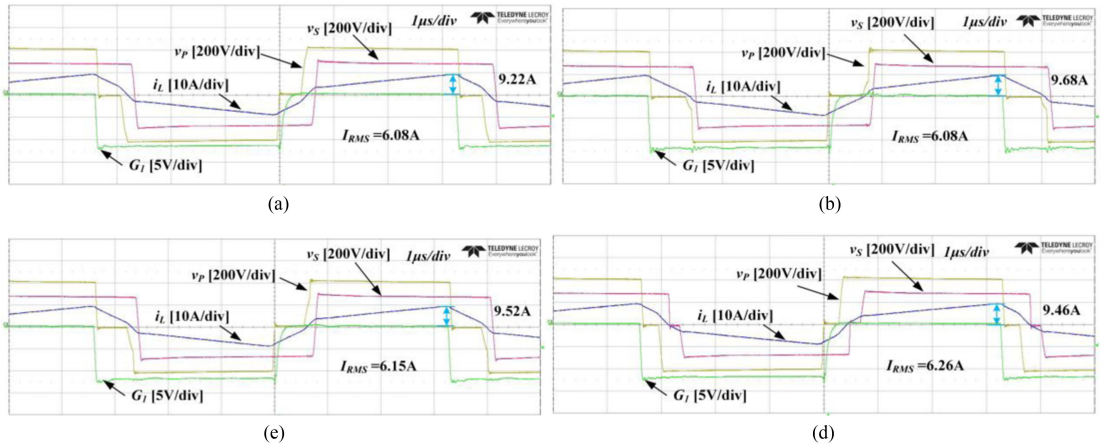

Fig. 5. Current stress and rms current comparison of optimized control strategy and NSGA2TPS. (a) $V_A = 400$ V, $V_B = 274.3$ V, and $m = 0.8$ in NSGA2TPS. (b) $V_A = 400$ V, $V_B = 274.3$ V, and $m = 0.8$ in TPS in [3]. (c) $V_A = 400$ V, $V_B = 274.3$ V, and $m = 0.8$ in UTPS in [9]. (d) $V_A = 400$ V, $V_B = 274.3$ V, and $m = 0.8$ in DPS in [6].

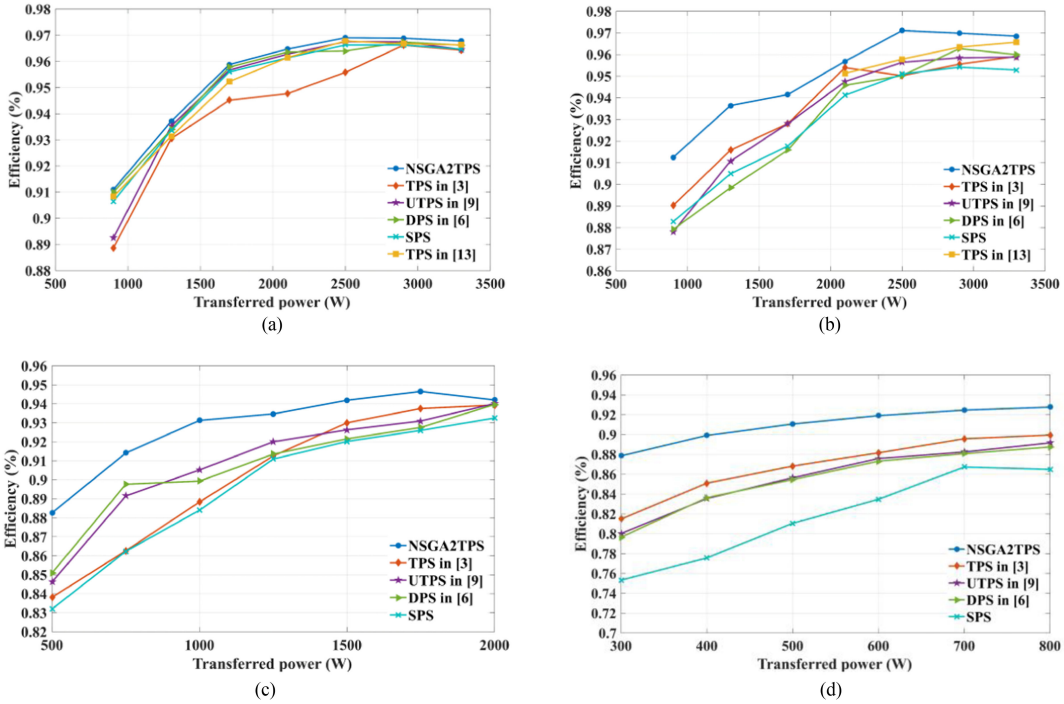

Fig. 6. Efficiency comparison at 25 °C ambient for various voltage gains m and output power with several control strategies. (a) $m = 0.9625$ ($V_A = 400$ V, $V_B = 330$ V). (b) $m = 0.8$ ($V_A = 400$ V, $V_B = 274.3$ V). (c) $m = 0.6$ ($V_A = 400$ V, $V_B = 205.7$ V). (d) $m = 0.4$ ($V_A = 400$ V, $V_B = 137.1$ V).

where $I_{\rm sp}$ and $I_{\rm ss}$ are the soft switching current boundaries on the primary side and secondary side, respectively, and $m' = 1 - m$. Mode 1 will replace Mode 4 as the optimal mode when $I_{(t2)}$ in Mode 4 approaches the secondary-side soft-switching boundary current. This means that Mode 4 is the optimal mode when

$$D_1 < m + \frac{4mf_S L}{m+1}\left(\frac{I_{sp}}{NV_B} - \frac{I_{ss}}{NV_A}\right). \tag{10}$$

The strategy for calculating phase shifts is shown in Fig. 4. The PI controller can adjust the dynamic response and correct any deviation of transferred power caused by circuit losses. D_3 adjustment is required to meet the target power in this control strategy. The value of D_3 is derived from the equation of transferred power in (2). The value of D_3 will not influence the ZVS requirement or minimum rms current. Prior work has set up lookup tables to implement control [5], [12]. The new phase-shift formulas—closed-form expressions that can be computed quickly—have broader application and can be implemented in real time by establishing two interrupt mechanisms: 1) a PWM interrupt and 2) a timer interrupt. The phase-shift duty ratios are calculated when the timer interrupt occurs. The timer

TABLE II
PARAMETERS OF THE DAB CONVERTER

Parameters	Value
Transformer turns ratio N	7:6
Inductance L	20 μH
Switching frequency f_s	150 kHz
Rated DC voltage V_A	400 V
Rated DC voltage V_B	330 V
Rated output power P_o	3.3 kW
Semiconductor switches	V22N65A

TABLE III
PERFORMANCE OF SPS AND PROPOSED TPS CONTROL STRATEGY

Control strategy	m	P_{trans} (W)	I_{rms} (A)	I_{stress} (A)	ZVS	Efficiency (%)
SPS	0.9625	3300	10.62	11.16	YES	0.9647
NSGA2TPS	0.9625	3300	9.59	11.92	YES	0.9678
SPS	0.9625	900	3.76	3.82	NO	0.9065
NSGA2TPS	0.9625	900	3.72	4.54	YES	0.9110
SPS	0.8	3300	11.84	17.66	YES	0.9529
NSGA2TPS	0.8	3300	11.08	16.73	YES	0.9685
SPS	0.8	900	4.93	8.62	NO	0.8828
NSGA2TPS	0.8	900	4.67	6.76	YES	0.9125
SPS	0.6	2000	11.88	19.8	NO	0.9325
NSGA2TPS	0.6	2000	9.81	14.69	YES	0.9421
SPS	0.6	750	8.09	14.64	NO	0.8664
NSGA2TPS	0.6	750	6.52	10.88	YES	0.9141
SPS	0.4	800	12.35	21.98	NO	0.8649
NSGA2TPS	0.4	800	7.33	13.16	YES	0.9277
SPS	0.4	300	11.13	19.44	NO	0.7533
NSGA2TPS	0.4	300	4.49	8.58	YES	0.8786

interrupt is triggered at the beginning of a user-defined time interval. Closed-form expressions do not need to be updated as parameters change, an important advantage compared to multidimension lookup tables.

IV. EXPERIMENTAL RESULTS

A DAB prototype has been prepared to test the method and control. Parameters are listed in Table II. To validate improvement, the TPS control strategy proposed in this letter has been compared with optimizing control strategies proposed in [3], [6], [9], and [13] and with single phase-shift control (SPS). Results for [6] are based on optimization of dual phase-shift control (DPS), Results for [3], [9], and [13] are based on optimization of TPS. Results for the operating state $V_A = 400$ V, $V_B = 274.3$ V, $m = 0.8$ are shown in Figs. 5(a)–(d).

Efficiency is compared for several optimized control strategies in Figs. 6(a)–(d). The results were obtained by running the published control strategies on this prototype. A comparison of rms current, peak current, and ZVS realization with the efficiency between SPS and the proposed TPS control for various voltage gains and power levels is given in Table III.

All these comparisons show that the results of the NSGA-II TPS control strategy proposed in this letter are best, and the advantage extends over a wide-load range. The farther the voltage gain is from 1, the greater the efficiency improvement with the proposed strategy. The TPS control proposed in this letter functions over the complete target voltage and power range, with reduced losses throughout the range, with an adaptive real-time implementation.

V. CONCLUSION

A multiobjective optimized TPS control strategy was presented for a DAB. Optimal solutions were identified by a genetic algorithm NSGA-II [15]. The resulting relationships led to closed-form TPS control solutions that can be implemented in real time across wide operating and load ranges. The optimization presented here enforces ZVS in both bridges, and seeks to minimize current and rms current. Experimental results validated the approach and demonstrated efficiency improvements across the operating range.

REFERENCES

[1] M. Yilmaz and P. T. Krein, "Review of the impact of vehicle-to-grid technologies on distribution systems and utility interfaces," *IEEE Trans. Power Electron.*, vol. 28, no. 12, pp. 5673–5689, Dec. 2013.

[2] L. Zhu, A. R. Taylor, G. Liu, and K. Bai, "A multiple-control for a SiC-based EV charger to optimize the light-load efficiency, current stress, and power quality," *IEEE J. Emerg. Sel. Top. Power Electron.*, vol. 6, no. 4, pp. 2262–2272, Dec. 2018.

[3] O. M. Hebala, A. A. Aboushady, K. H. Ahmed, and I. Abdelsalam, "Generic closed-loop controller for power regulation in dual active bridge dc–dc converter with current stress minimization," *IEEE Trans. Ind. Electron.*, vol. 66, no. 6, pp. 4468–4478, Jun. 2019.

[4] H. Shi, H. Wen, Y. Hu, and L. Jiang, "Reactive power minimization in bidirectional dc–dc converters using a unified-phasor-based particle swarm optimization," *IEEE Trans. Power Electron.*, vol. 33, no. 12, pp. 10990–11006, Dec. 2018.

[5] F. Krismer and J. W. Kolar, "Closed form solution for minimum conduction loss modulation of DAB converters," *IEEE Trans. Power Electron.*, vol. 27, no. 1, pp. 174–188, Jan. 2012.

[6] B. Zhao, Q. Song, W. Liu, and W. Sun, "Current-stress-optimized switching strategy of isolated bidirectional dc–dc converter with dual-phase-shift control," *IEEE Trans. Ind. Electron*, vol. 60, no. 10, pp. 4458–4467, Oct. 2013.

[7] Z. Qin, Y. Shen, P. C. Loh, H. Wang, and F. Blaabjerg, "A dual active bridge converter with an extended high-efficiency range by dc blocking capacitor voltage control," *IEEE Trans. Power Electron.*, vol. 33, no. 7, pp. 5949–5966, Jul. 2018.

[8] A. Tong, L. Hang, G. Li, X. Jiang, and S. Gao, "Modeling and analysis of a dual-active-bridge-isolated bidirectional dc/dc converter to minimize RMS current with whole operating range," *IEEE Trans. Power Electron.*, vol. 33, no. 6, pp. 5302–5316, Jun. 2018.

[9] J. Huang, Y. Wang, Z. Li, and W. Lei, "Unified triple-phase shift control to minimize current stress and achieve full soft-switching of isolated bidirectional dc–dc converter," *IEEE Trans. Ind. Electron.*, vol. 63, no. 7, pp. 4169–4179, Jul. 2016.

[10] H. Shi *et al.*, "Minimum-backflow-power scheme of DAB-based solid-state transformer with extended-phase-shift control," *IEEE Trans. Ind. Appl.*, vol. 54, no. 4, pp. 3483–3496, Jul./Aug. 2018.

[11] N. Hou, W. Song, and M. Wu, "Minimum-current-stress scheme of dual active bridge dc–dc converter with unified phase-shift control," *IEEE Trans. Power Electron.*, vol. 31, no. 12, pp. 8552–8561, Dec. 2016.

[12] J. Everts, "Closed-form solution for efficient ZVS modulation of DAB converters," *IEEE Trans. Power Electron.*, vol. 32, no. 10, pp. 7561–7576, Oct. 2017.

[13] K. Shen *et al.*, "ZVS control strategy of dual active bridge dc/dc converter with triple-phase-shift modulation considering RMS current optimization," *J. Eng.*, vol. 2019, no. 18, pp. 4708–4712, 2019.

[14] F. Xue, R. Yu, and A. Q. Huang, "A 98.3% efficient GaN isolated bidirectional dc–dc converter for dc microgrid energy storage system applications," *IEEE Trans. Ind. Electron.*, vol. 64, no. 11, pp. 9094–9103, Nov. 2017.

[15] K. Deb, A. Pratap, S. Agarwal, and T. Meyarivan, "A fast and elitist multiobjective genetic algorithm: NSGA-II," *IEEE Trans. Evol. Comput.*, vol. 6, no. 2, pp. 182–197, Apr. 2002.

[16] K. Deb and R. B. Agrawal, "Simulated binary crossover for continuous search space," *Complex Syst.*, vol. 9, no. 2, pp. 115–148, Apr. 1995.

[17] J. Everts, F. Krismer, J. Van den Keybus, J. Driesen, and J. W. Kolar, "Optimal ZVS modulation of single-phase single-stage bidirectional DAB ac–dc converters," *IEEE Trans. Power Electron*, vol. 29, no. 8, pp. 3954–3970, Aug. 2014.